Supporting Information of Theoretical Design and Experimental Realization of Fe^{3+}-Doped Dual-Band Near-Infrared Garnet Phosphors

Yutong Wang,[1,*] Anfei Chen,[2,3,4,*] Sha Jiang,[1,†] Lei Zhong,[5] Li Li,[1] Xianju Zhou,[1] Chang-Kui Duan,[2,3,4,6] and Qiaoling Chen[2,3,4,‡]

[1] *School of Science, Chongqing University of Posts and Telecommunications, Chongqing 400065, PR China*

[2] *CAS Key Laboratory of Microscale Magnetic Resonance, and School of Physical Sciences, University of Science and Technology of China, Hefei 230026, China*

[3] *Anhui Province Key Laboratory of Scientific Instrument Development and Application, University of Science and Technology of China, Hefei 230026, China*

[4] *CAS Center for Excellence in Quantum Information and Quantum Physics, University of Science and Technology of China, Hefei 230026, China*

[5] *School of Chemical Engineering and Technology, Sun Yat-sen University, Zhuhai 519082, China*

[6] *Hefei National Laboratory, University of Science and Technology of China, Hefei 230088, China*

(Dated: December 10, 2024)

Note S1 Computational settings and discussions on the defect formation energies in the series garnets

All first-principles calculations were performed based on the density functional theory (DFT) implemented in the VASP code [1, 2]. The recommended projector augmented wave (PAW) method [3] was adopted to treat the interaction between ion core and electrons and the generalized gradient approximation of the Perdew-Burke-Ernzerhof (PBE) functional [4] was used for the exchange correlation functional. The GGA+U scheme was applied to correct the orbital-dependent potential of transition metal ions and $U_{\text{eff}} = 3$ eV was used for the Fe–3d orbitals. The conjugate gradient method was used to perform the geometric optimization until the Hellmann-Feynman forces on atoms were less than 0.01 eV/Å. The crystal hosts were optimized with an energy cutoff of 400 eV. The defect calculations were performed based on the supercell method, and the unitcell of garnet host containing 160 ions was sufficiently dilute for the defect modeling. The formation energy calculations were conducted at the GGA+U level to discuss the native defects, site occupation and valence states of iron dopants; whereas the optical transition energies were performed at the HSE06 level. Such calculations have been widely applied in a large variety of systems [5–7].

We followed the standard defect scheme as outlined by Freysoldt et al. [6], where the formation energy of a defect X in charge state q is defined as

$$E^f[X^q] = E_{\text{tot}}[X^q] + E_{\text{corr}}[X^q] - E_{\text{tot}}[\text{bulk}] - \sum_i n_i\mu_i + qE_{\text{F}}, \tag{1}$$

where $E_{\text{tot}}[X^q]$ and $E_{\text{tot}}[\text{bulk}]$ are the total energies of the supercell containing the X^q defect and the perfect supercell, respectively. n_i indicates the number change of type i atom that have been added to (n_i>0) or removed from (n_i<0) the perfect supercell to form the X^q defect. μ_i is the chemical potential of type i atom species, and E_{F} is the electronic Fermi energy. Generally, $E_{\text{corr}}[X^q]$ is a *post hoc* small correction to the total energy of the charged defect, and it is ignored here due to the its negligible influence on the valence state and site occupation of iron impurities.

The chemical potentials μ_i are specified with respect to their μ_i^0 values of the stable

* Y. Wang and A. Chen contributed equally to this work, from experimental and theoretical aspects, respectively.

† jiangsha@cqupt.edu.cn

‡ Cql@ustc.edu.cn

phases as $\mu_i = \mu_i^0 + \Delta\mu_i$. In $A_3B_2C_3O_{12}$, the relative chemical potential of raw materials are restricted by competing secondary compounds of ternary oxides, as shown in Fig. S1(a)–S3(a). Combining with the estimation of oxygen chemical potential of $\mu_O = \frac{1}{2}E_{O_2} + \Delta\mu_O = \frac{1}{2}E_{O_2} + \frac{1}{2}k_BT[\ln(\frac{pV_Q}{k_BT}) - \ln Z_{rot} - \ln Z_{vib}]$, the elemental chemical potentials and the defect formation energies can be determined by the set $[\Delta\mu_{AO}, \Delta\mu_{B_2O_3}, \Delta\mu_{CO_2}, \Delta\mu_O]$. Besides, the chemical potential of Fe μ_{Fe} is determined by fixing the total calculated concentrations of Fe defects to the experimental doping concentration of 1% and the μ_{Fe} should ensure that the potential Fe-related phases are depleted.

In the series $Sr_3Sc_2Ge_3O_{12}$, $Sr_3Lu_2Ge_3O_{12}$, and $Sr_3Y_2Ge_3O_{12}$ garnets, the formation energies of native defects and iron dopants are calculated, and the influence of chemical potentials is discussed, as shown in Fig. S1–S3.

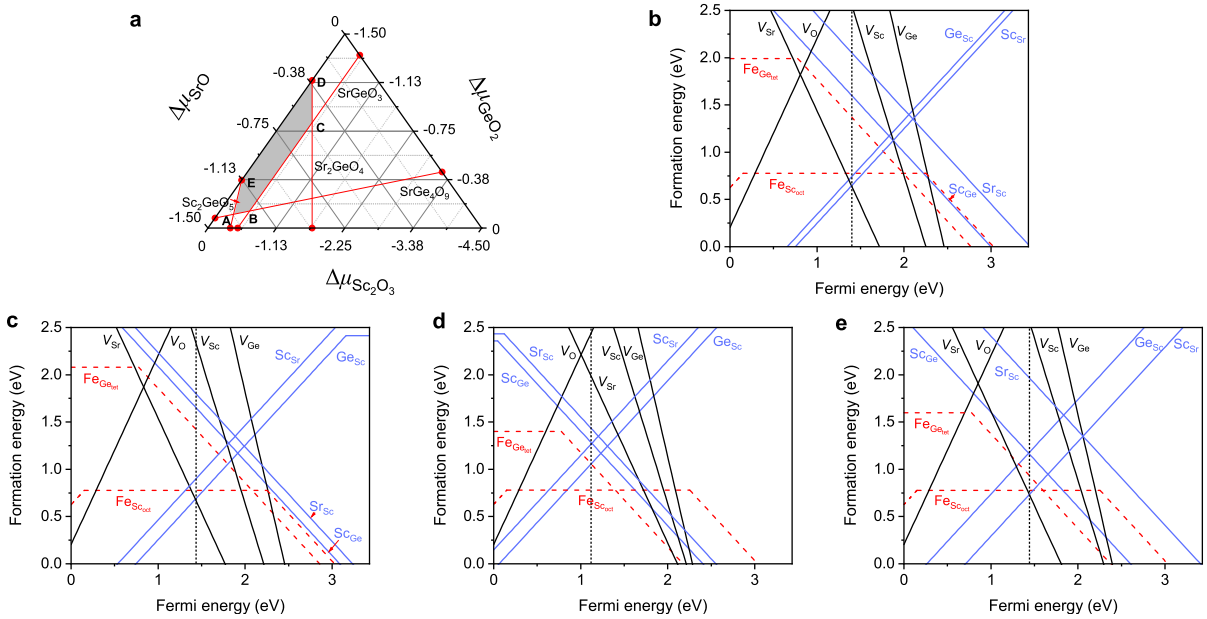

FIG. S1. (a) Allowed chemical potential range of $Sr_3Sc_2Ge_3O_{12}$ host. (b–e) Formation energies of intrinsic defects and iron dopants as functions of Fermi energy in the chemical potential conditions of A, B, C and E points in (a) and moderate oxygen atmosphere $\Delta\mu_O = -1.5$ eV, respectively. Defect formation energies as function of Fermi nergy in the chemical potential condition of D point are shown in Fig. 1(e) of the main text.

Note S2 Experimental details

Synthesis A series of $Sr_3Sc_2Ge_3O_{12}$: $x\%Fe^{3+}$ (x = 0.1, 0.5, 1, 3, 5, 7), $Sr_3Lu_2Ge_3O_{12}$: $0.5\%Fe^{3+}$ and $Sr_3Y_2Ge_3O_{12}$: $0.5\%Fe^{3+}$ phosphors were fabricated by high-temperature solid-

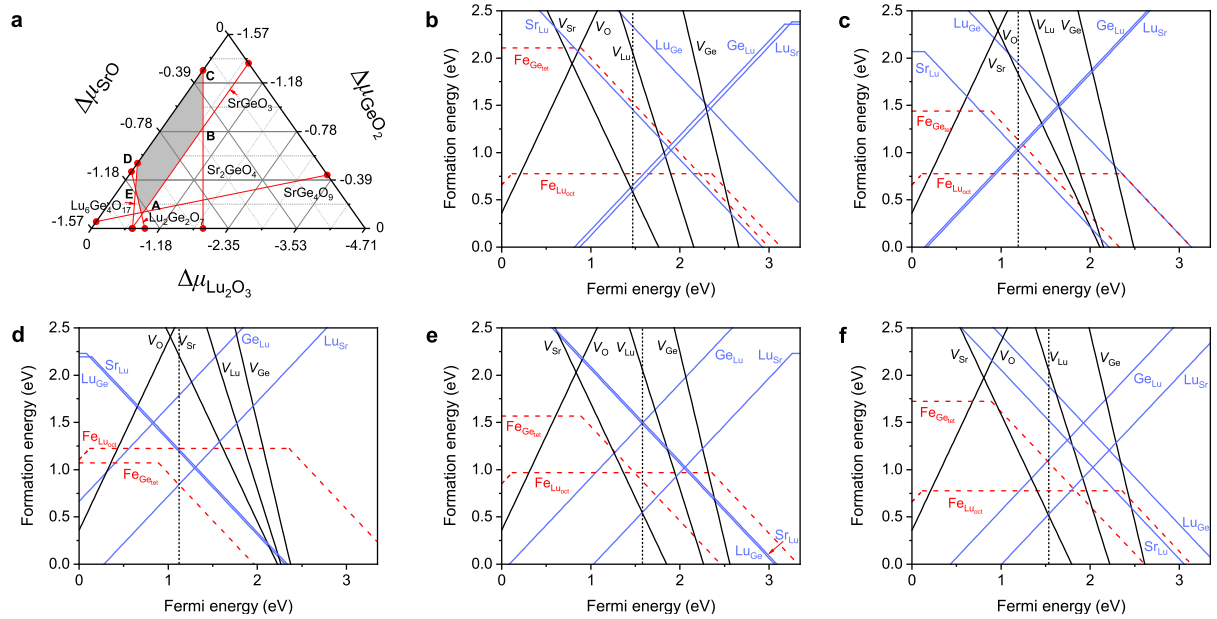

FIG. S2. (a) Allowed chemical potential range of $Sr_3Lu_2Ge_3O_{12}$ host. (b–f) Formation energies of intrinsic defects and iron dopants as functions of Fermi energy in the chemical potential conditions of $A-E$ points in (a) and moderate oxygen atmosphere $\Delta\mu_O = -1.5$ eV, respectively.

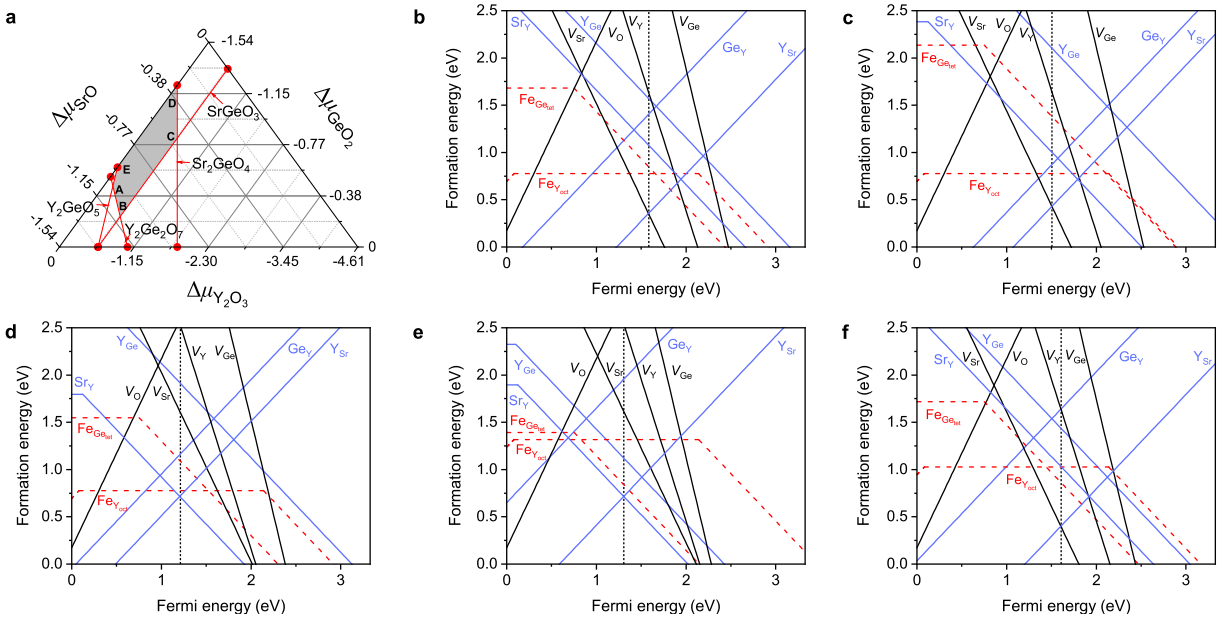

FIG. S3. (a) Allowed chemical potential range of $Sr_3Y_2Ge_3O_{12}$ host. (b–f) Formation energies of intrinsic defects and iron dopants as functions of Fermi energy in the chemical potential conditions of $A-E$ points in (a) and moderate oxygen atmosphere $\Delta\mu_O = -1.5$ eV, respectively.

state reaction from the following raw materials: $SrCO_3$ (Aladdin, AR), Sc_2O_3 (Aladdin, 99.9%), GeO_2 (Aladdin, 99.99%), Lu_2O_3 (Aladdin, 99.99%), Y_2O_3(Sinopharm Chemical

TABLE S1. The Fe–O bond lengths $L(Fe^{3+} - O)$ (in units of Å) and O–Fe–O bond angles $A(O - Fe^{3+} - O)$ of tetrahedral $[FeO_4]^{5-}$ in garnets.

	$Sr_3Sc_2Ge_3O_{12}$	$Sr_3Lu_2Ge_3O_{12}$	$Sr_3Y_2Ge_3O_{12}$
$L(Fe^{3+} - O)$	1.894	1.899	1.901
	1.894	1.899	1.901
	1.894	1.899	1.901
	1.894	1.899	1.901
$A(O - Fe^{3+} - O)$	113.91°	114.53°	115.05°
	113.91°	114.53°	115.05°
	113.91°	114.53°	115.05°
	113.91°	114.53°	115.05°
	100.92°	99.77°	98.82°
	100.92°	99.77°	98.82°

TABLE S2. The transition energies of $Fe_{Sc}^{\times}$ with and without the perturbation of a nearby intrinsic $Sc_{Sr}^{\bullet}$ defect (the charge compensator of the Fe'_{Ge} defect) the in SSGG host (in units of eV).

SSGG	$Fe_{Sc}^{\times}$	$Fe_{Sc}^{\times} + Sc_{Sr}^{\bullet}$
Exc.	1.365	1.306
Emi.	1.192	1.107
Stokes	0.173	0.199

Reagent, Shanghai, 99.99%) and Fe_2O_3(Rhawn Reagent, Shanghai, AR). H_3BO_3(Aladdin, AR) was added as a flux ingredient. The corresponding raw materials were thoroughly mixed in an agate mortar using alcohol as the mixing medium. The powders were calcined in a furnace at 1200 °C for 10 h in air. Finally, the products were cooled to room temperature and ground again for further characterization.

Characterization X-ray powder diffraction experiment was performed at ambient condition on a XD-2 diffractometer (Persee Analytics, China) with Cu-Kα radiation (λ = 1.5406 Å) operating at 36 kV and 20 mA. Diffraction data were collected in the 2θ range between 10° and 80° with the scanning rate of 2°/min. The morphology and the element mapping of the $Sr_3Sc_2Ge_3O_{12} : Fe^{3+}$ sample were achieved on a field emission scanning electron microscope (SEM, Apreo 2S HiVac, Thermo Fisher Scientific) with an energy spectrometer (Escalab 250Xi, Thermo Fisher Scientific). The X-ray photoelectron spectroscopy spectra were measured via a spectrometer (Escalab Qxi, Thermo Fisher Scientific). The photoluminescence (PL), photoluminescence excitation (PLE) spectra and luminescence decay curves at different temperatures were recorded at an a steady-state/transient fluores-

cence spectrometer FLS1000 (Edinburgh Instruments, UK) equipped with a 450 W xenon lamp. The temperature controller X-1AL (ARS inc., USA) cryostat equipped with a powder chamber was used and the interval for the measurements was not less than 10 min in order to achieve thermal equilibrium. The quantum efficiency of the sample is measured on the Quantaurus-QY Plus UV-NIR absolute PL quantum yield spectrometer (C13534-11, Hamamatsu Photonics).

The integral quantum efficiency (IQE) of luminescence can be calculated using the following equation:

$$\mathrm{IQE} = \frac{\mathrm{L_S} - \mathrm{L_R}}{\mathrm{E_R} - \mathrm{E_S}} \times 100\% \tag{2}$$

where $\mathrm{E_R}$ and $\mathrm{E_S}$ represent the integrated intensity of the $BaSO_4$ reference and phosphor sample respectively, corresponding to the excitation spectra. Similarly, $\mathrm{L_R}$ and $\mathrm{L_S}$ represent the integrated intensity of the $BaSO_4$ reference and phosphor sample respectively, related to the emission spectra. Furtherly, the absorption efficiency (AE) and external quantum efficiency (EQE) can be calculated by using the following equations:

$$\mathrm{AE} = \frac{\mathrm{E_R} - \mathrm{E_S}}{\mathrm{E_R}} \times 100\% \tag{3}$$

$$\mathrm{EQE} = \mathrm{IQE} \times \mathrm{AE} = \frac{\mathrm{L_S} - \mathrm{L_R}}{\mathrm{E_R}} \times 100\% \tag{4}$$

Due to instrument limitations, the emission spectra can only be detected below 957 nm. The quantum efficiency is estimated by considering the uncovered S2 part [8]. At an excitation wavelength of 274 nm, the IQE and EQE of the sample are estimated to be 14.1% and 9.6% respectively, and the IQE and EQE are estimated to be 11.4% and 7.1% respectively when sample is excited by 302 nm.

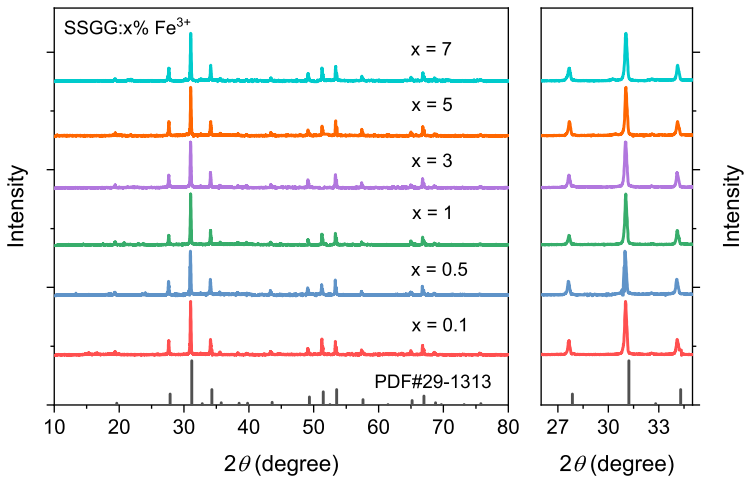

FIG. S4. XRD patterns of $Sr_3Sc_2Ge_3O_{12}$:x%Fe ($x = 0.1, 0.5, 1, 3, 5, 7$) phosphors.

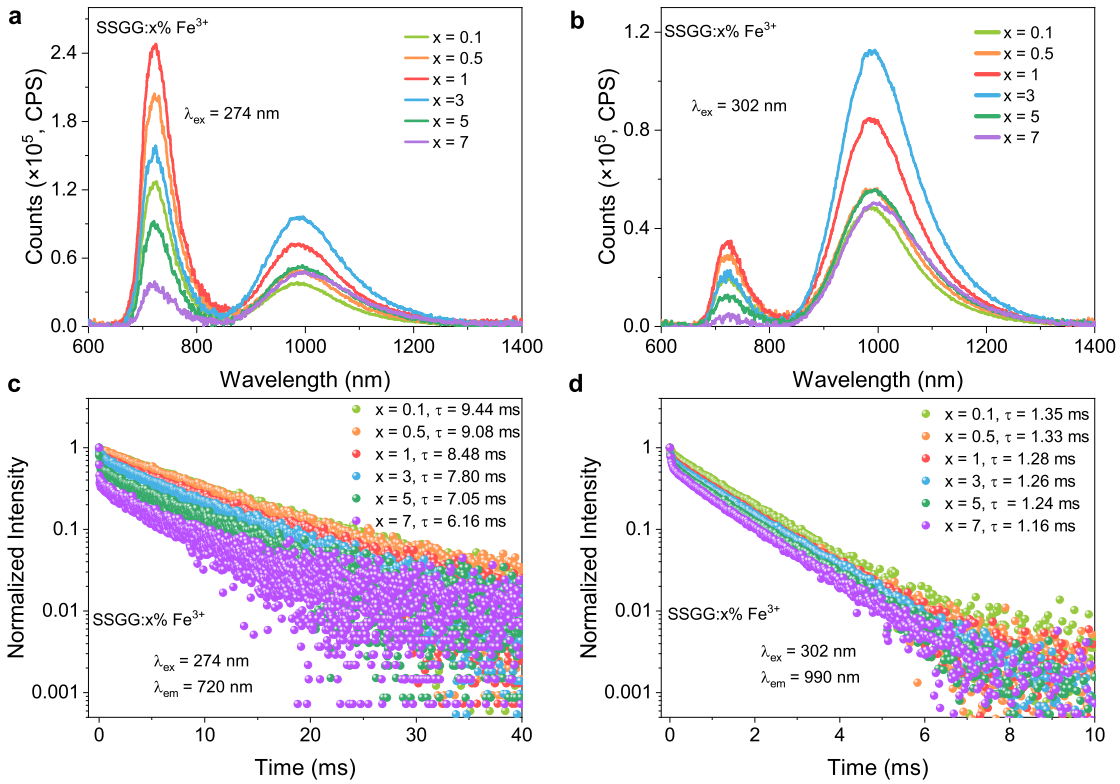

FIG. S5. PL spectra of $Sr_3Sc_2Ge_3O_{12}$: x%Fe ($x = 0.1, 0.5, 1, 3, 5, 7$) under $\lambda_{ex} = 274$ nm (a) and $\lambda_{ex} = 302$ nm (b) excitaions, and the luminescent decay curves monitoring $\lambda_{em} = 720$ nm (c) and $\lambda_{em} = 990$ nm (d).

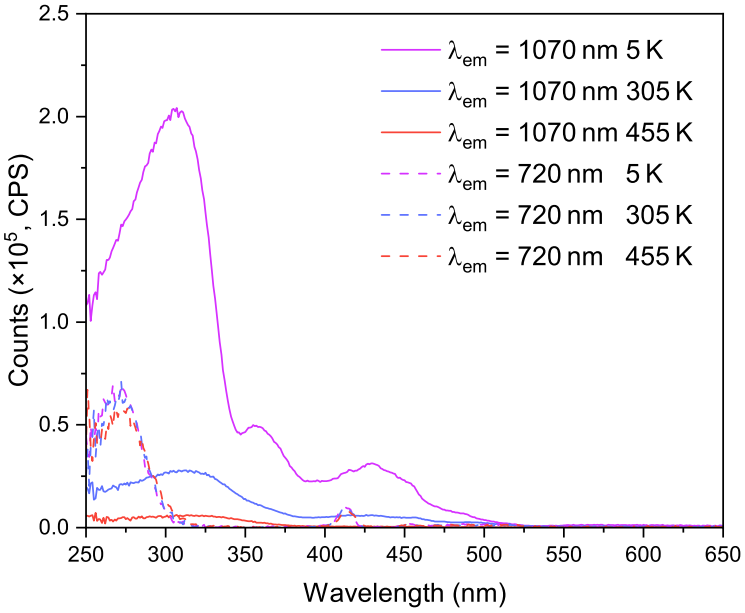

FIG. S6. The PLE spectra at 5 K, 305 K and 455 K when monitoring 1070 nm (solid lines) and 720 nm (dashed lines) luminescence in SSGG:1%Fe samples.

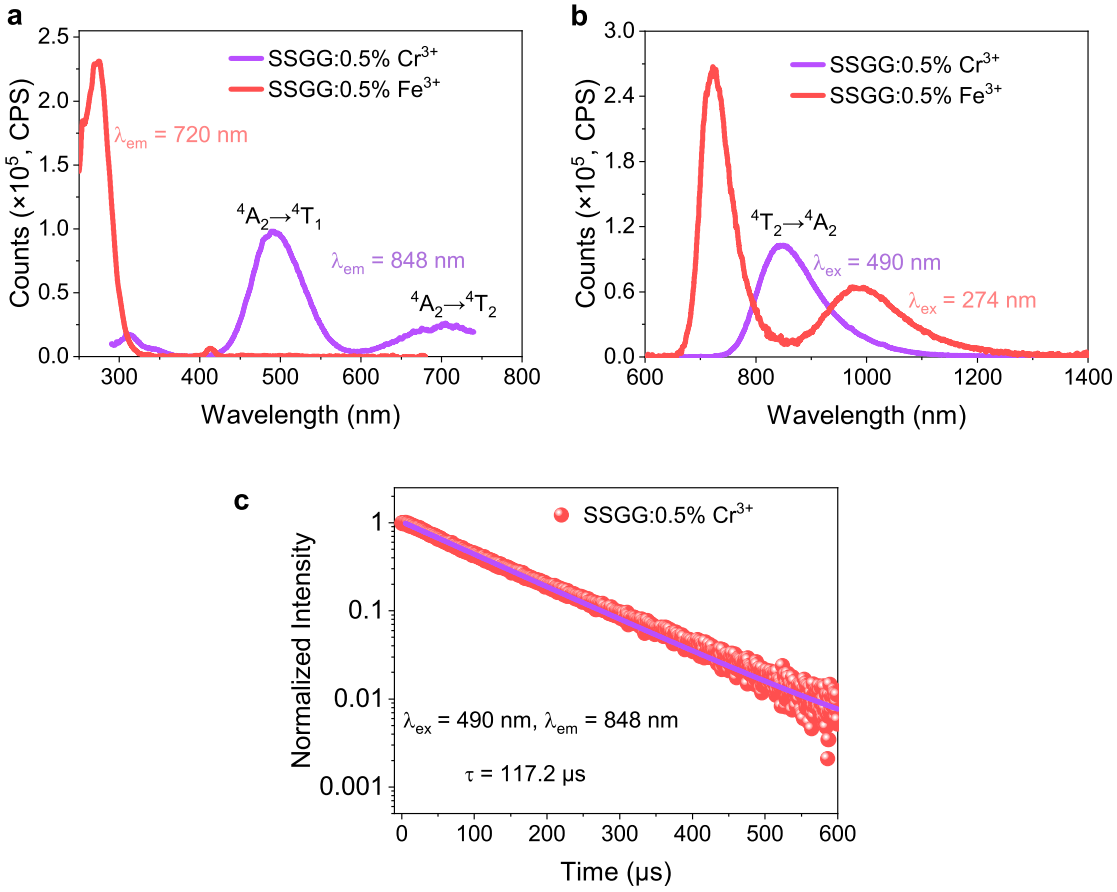

FIG. S7. The PL excitation (a), PL spectra (b) and luminescent decay curve (c) of $Sr_3Sc_2Ge_3O_{12}$:0.5%Cr^{3+} and $Sr_3Sc_2Ge_3O_{12}$:0.5%Fe^{3+}.

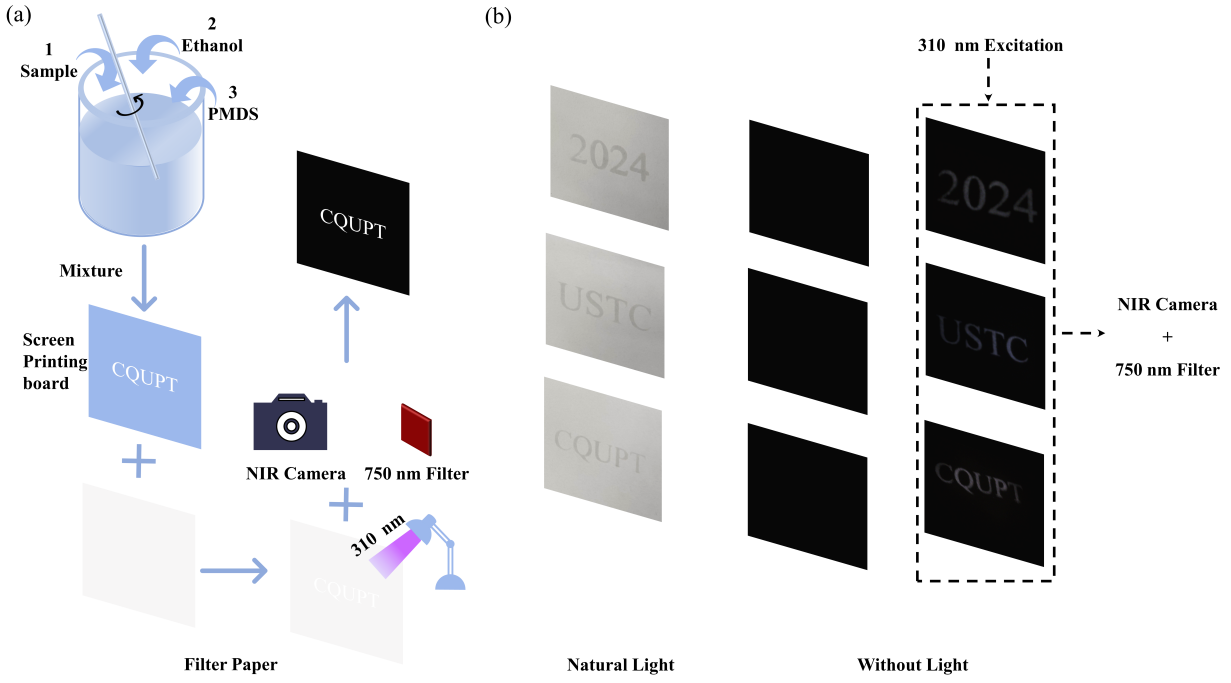

FIG. S8. (a) The scheme of producing anti-counterfeiting labels using screen printing; (b) Photos taken in natural light by a visible light camera (left), and photos taken in a dark environment without (middle) and with (right) the 310 excitation by a near-infrared camera.

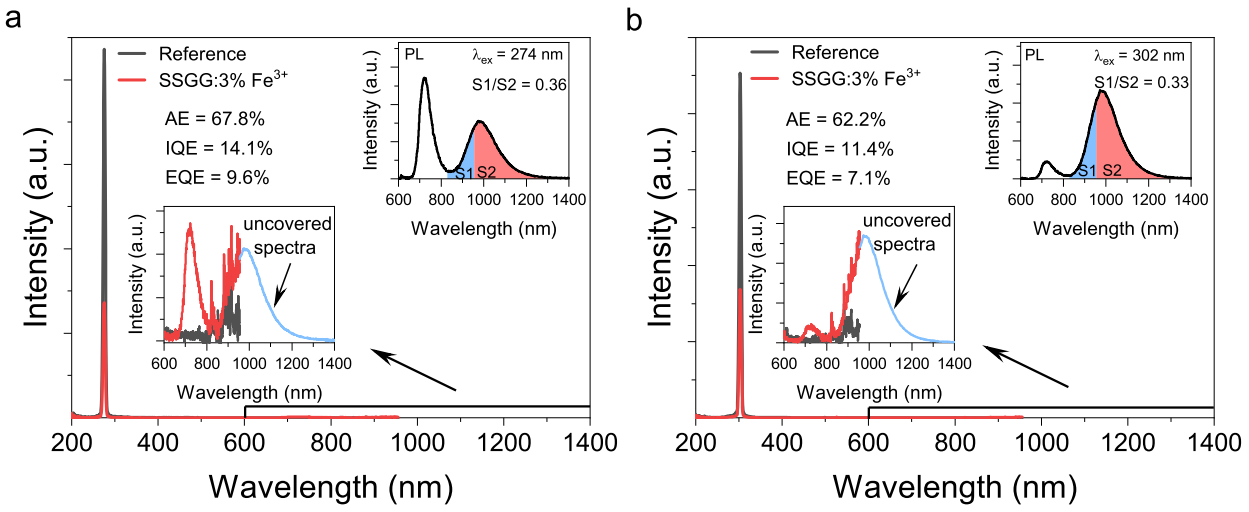

FIG. S9. The quantum efficiency of SSGG: 3%Fe^{3+} excited by 274 nm (a) and 302 nm (b). (The insets show the amplified emission spectra (bottom left corner), covered part S1 and uncovered part S2 in NIR II region (top right corner)).

TABLE S3. Working temperature and relative sensitivity of luminescence decay time-based thermometers for various activators. YAG and GC stand for $Y_3Al_5O_{12}$ and glass ceramic, respectively.

Activator	Host material	Temperature (K)	Relative sensitivity (% K^{-1})	Ref.
Fe^{3+}	$Sr_3Sc_2Ge_3O_{12}$	80–300	1.24 (155 K)	This work
	$NaScSi_2O_6$	293–423	3.46 (423 K)	[9]
Mn^{2+}	Zn_2GeO_4	250–420	12.2 (370 K)	[10]
Mn^{3+}	Mn^{4+}, Nd^{3+}: YAG	200–400	2.69 (ca. 300 K)	
Mn^{4+}	β-Li_2TiO_3	10–350	3.21 (332 K)	
	$Li_4Ti_5O_{12}$	10–350	2.6 (330 K)	
Cr^{3+}	Bi^{3+}: $ZnGa_2O_4$	293–473	0.3	
	YF_3 + Ga_2O_3 GC	300–550	0.59 (386 K)	[11]
Eu^{3+}	SrY_2O_4	293–473	0.34 (473 K)	
	BaY_2ZnO_5	330–510	2.2 (490 K)	
Yb^{3+}	Nd^{3+}:$NaGdF_4$	/	1.59 (343 K)	[12]

[1] G. Kresse and J. Hafner, Ab initio molecular dynamics for liquid metals, Phys. Rev. B **47**, 558 (1993).

[2] G. Kresse and J. Hafner, Ab initio molecular-dynamics simulation of the liquid-metal–amorphous-semiconductor transition in germanium, Phys. Rev. B **49**, 14251 (1994).

[3] P. E. Blöchl, Projector augmented-wave method, Phys. Rev. B **50**, 17953 (1994).

[4] J. P. Perdew, K. Burke, and M. Ernzerhof, Generalized gradient approximation made simple, Phys. Rev. Lett. **77**, 3865 (1996).

[5] Q. Chen, M. Liu, L. Shang, and C.-K. Duan, Elucidating the multisite and multivalence nature of mn ions in solids and predicting their optical transition properties: A case study on a series of garnet hosts, Inorg. Chem. **61**, 18690 (2022).

[6] C. Freysoldt, B. Grabowski, T. Hickel, J. Neugebauer, G. Kresse, A. Janotti, and C. G. Van de Walle, First-principles calculations for point defects in solids, Rev. Mod. Phys. **86**, 253 (2014).

[7] Z. Feng and C.-K. Duan, Understanding photoluminescence of bismuth-doped ternary alkaline earth d^{10} metal oxides via first-principles calculations, Phys. Rev. B **107**, 085144 (2023).

[8] Y. Wang, Z. Wang, G. Wei, Y. Yang, S. He, J. Li, Y. Shi, R. Li, J. Zhang, and P. Li, Ultra-Broadband and high efficiency Near-Infrared $Gd_3Zn_xGa_{5-2x}Ge_xO_{12}$:$Cr^{3+}$ (x =0–2.0) garnet phosphors via crystal field engineering, Chem. Eng. J. **437**, 135346 (2022).

[9] X. Zhang, D. Chen, X. Chen, C. Zhou, P. Chen, Q. Pang, and L. Zhou, Broadband near-infrared luminescence from Fe^{3+}-activated $NaScSi_2O_6$ phosphors for luminescence thermometry and night-vision applications, Dalton Trans. **51**, 14243 (2022).

[10] F. Chi, B. Jiang, Z. Zhao, Y. Chen, X. Wei, C. Duan, M. Yin, and W. Xu, Multimodal temperature sensing using $Zn_2GeO_4 : Mn^{2+}$ phosphor as highly sensitive luminescent thermometer, Sens. Actuators B Chem. **296**, 126640 (2019).

[11] D. Chen, Z. Wan, Y. Zhou, X. Zhou, Y. Yu, J. Zhong, M. Ding, and Z. Ji, Dual-phase glass ceramic: Structure, dual-modal luminescence, and temperature sensing behaviors, ACS Appl. Mater. Interfaces **7**, 19484 (2015).

[12] Z. Ji, Y. Cheng, X. Cui, H. Lin, J. Xu, and Y. Wang, Heating-induced abnormal increase in Yb^{3+} excited state lifetime and its potential application in lifetime luminescence nanothermometry, Inorg. Chem. Front. **6**, 110 (2019).